JACS Au
AN OPEN ACCESS JOURNAL OF THE AMERICAN CHEMICAL SOCIETY

pubs.acs.org/jacsau
Article

DNA Nanoribbon-Assisted Intracellular Biosynthesis of Fluorescent Gold Nanoclusters for Cancer Cell Imaging

Xiangyuan Ouyang,*[,‖] Nan Jia,[‖] Jing Luo,[‖] Le Li,[‖] Jiangshan Xue, Huaiyu Bu,* Gang Xie, and Ying Wan*

Cite This: JACS Au 2023, 3, 2566−2577
Read Online
ACCESS | Metrics & More | Article Recommendations | Supporting Information

ABSTRACT: Metal nanoclusters (NCs) have emerged as a promising class of fluorescent probes for cellular imaging due to their high resistance to photobleaching and low toxicity. Nevertheless, their widespread use in clinical diagnosis is limited by their unstable intracellular fluorescence. In this study, we develop an intracellularly biosynthesized fluorescent probe, DNA nanoribbon-gold NCs (DNR/AuNCs), for long-term cellular tracking. Our results show that DNR/AuNCs exhibit a 4-fold enhancement of intracellular fluorescence intensity compared to free AuNCs. We also investigated the mechanism underlying the fluorescence enhancement of AuNCs by DNRs. Our findings suggest that the higher synthesis efficiency and stability of AuNCs in the lysosome may contribute to their fluorescence enhancement, which enables long-term (up to 15 days) fluorescence imaging of cancer cells (enhancement of ∼60 times compared to free AuNCs). Furthermore, we observe similar results with other metal NCs, confirming the generality of the DNR-assisted biosynthesis approach for preparing highly bright and stable fluorescent metal NCs for cancer cell imaging.

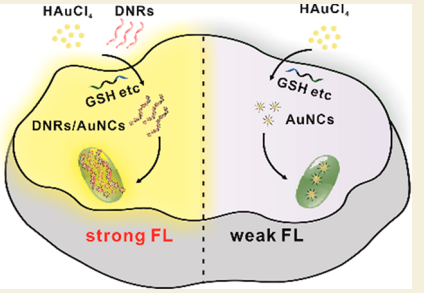

KEYWORDS: *metal nanoclusters, DNA nanostructures, self-assembly, biosynthesis, fluorescence imaging*

INTRODUCTION

Currently, fluorescent probes, including organic fluorescent dyes,[1−3] semiconductor quantum dots,[4−6] fluorescent proteins,[7−10] and upconversion nanomaterials,[11−13] are commonly used for intracellular fluorescence imaging because of their high luminescence and photostability.[14−16] However, these fluorescent probes may suffer from limitations in making reliable intracellular measurements. For example, several organic dyes exhibit small Stokes shifts and poor photobleaching resistance.[17,18] Penetrating cell membranes is hard for semiconductor quantum dots with large size, and most of them are toxic.[19] Fluorescent proteins are easily denatured,[20] and the rare earth upconversion nanoparticles exhibit poor biocompatibility.[21] These disadvantages limit the application of the fluorescent probes currently used in the bioimaging field.

Fluorescent metal nanoclusters (NCs) have been widely used for live-cell imaging in the past decade because of their ultrasmall size, good biocompatibility, low toxicity, large Stokes shifts, and excellent stability against photobleaching.[22−24] Among the metal NC-based bioimaging methods, intracellular biosynthesis of metal NCs has achieved remarkable success in recent years due to their easy synthesis and excellent cellular targeting.[25−28] However, the widespread use of these individual metal NCs in clinical diagnosis is limited by their unstable intracellular fluorescence,[29−31] which is crucial for long-term tracking and real-time observation of dynamic cell migration, division, and lysis to gain deeper insights into tumor pathogenesis.[32−37]

Compared with individual metal NCs, metal NC assembly-based imaging probes can effectively enhance their fluorescence stability, eventually prolonging the imaging time in tumor sites.[38−42] A series of self-assembly strategies were developed through electrostatic interactions,[43,44] $\pi-\pi$ stacking,[45,46] hydrophobic interactions,[47,48] and so on. However, the fluorescence imaging performances of these assemblies were still unsatisfactory due to their limited ability to penetrate the cell membrane. This limitation arises from the fact that they are formed prior to entering the cell, leading to a significant effect on the cellular uptake rate.

Since the emergence of DNA nanotechnology, self-assembled DNA nanostructures have demonstrated considerable promise in numerous biomedical theranostic applications because of their excellent programmability and biocompatibility.[49−55] Many studies have shown that the intracellular GSH level in tumor cells is as high as 2−20 mM, which is 100−1000 times and 7−10 times than that of the extracellular matrix and normal tissues, respectively.[56,57] Herein, for the first time, we proposed the cancer cell biosynthesis and assembly of fluorescent gold NCs (AuNCs)

Received: July 8, 2023
Revised: August 2, 2023
Accepted: August 7, 2023
Published: September 6, 2023

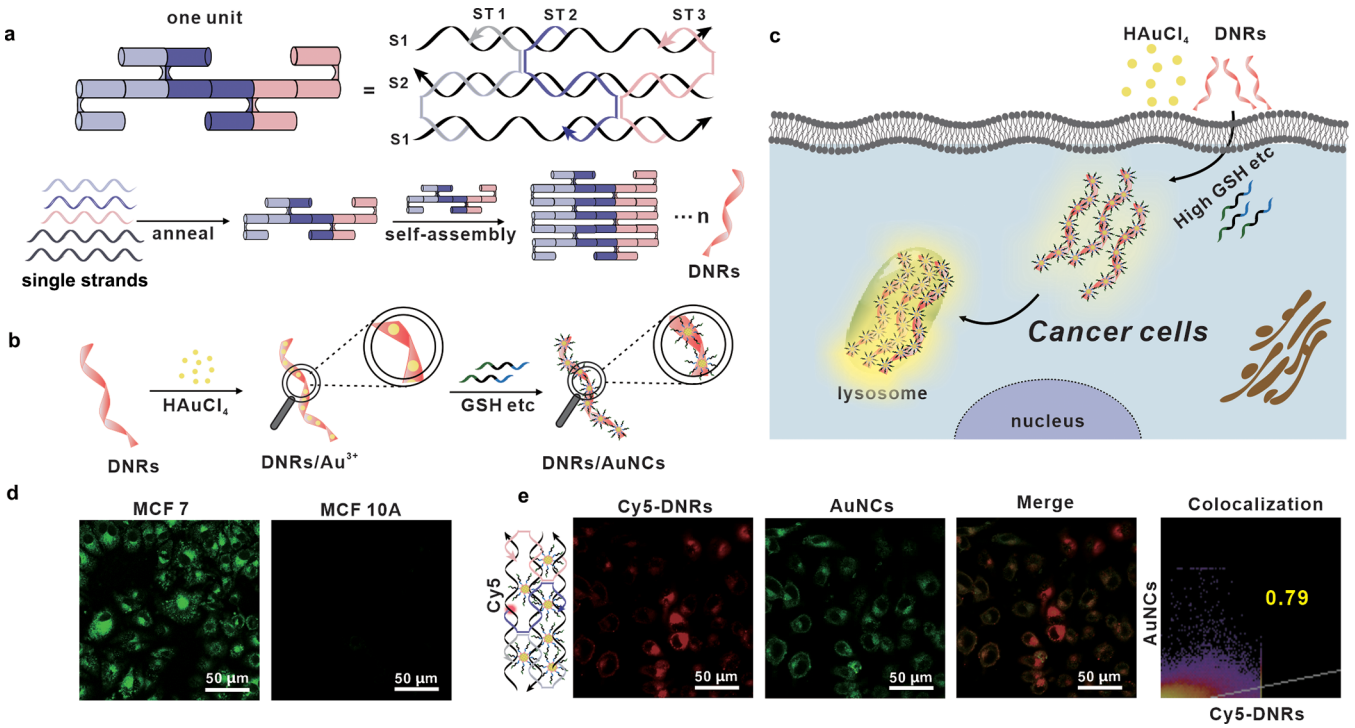

Figure 1. (a) Schematic diagram of DNRs. (b) Schematic illustration of the synthesis procedure of DNRs/AuNCs. (c) Biosynthesis of DNRs/AuNCs in cancer cells. (d) Laser confocal fluorescence images of DNRs/Au^{3+} incubated with MCF 7 cells and MCF 10A cells for 24 h. (e) Laser confocal fluorescence images of AuNCs colocalized with Cy5-DNRs. DNRs/Au^{3+} was incubated with MCF 7 cells for 24 h.

assisted by DNA nanoribbons (DNRs) to realize long-term cellular tracking. It is worth mentioning that, unlike the previously reported work, the assembly of AuNCs in this study is carried out intracellularly rather than extracellularly. This approach effectively resolves the challenge of large particle penetration into the cell membrane. We demonstrated that the synthesis of AuNCs with DNRs as the template (DNRs/AuNCs) can significantly improve the intracellular fluorescence intensity of the resultant AuNCs compared with those AuNCs synthesized without the DNRs templates (the maximum enhancement of ∼4 times was observed). Inductively coupled plasma mass spectrometry (ICP-MS) and fluorescence colocalization techniques revealed that DNRs facilitated the intracellular biosynthesis of AuNCs and enhanced the stability of AuNCs in the lysosome, which may account for the fluorescence enhancement. Importantly, this strategy was also successful in the case of other metal NCs, indicating that DNR-assisted biosynthesis can be a general approach for preparing high-performance fluorescent probes for intracellular imaging.

RESULTS AND DISCUSSION

In order to enter cells, both single and double-stranded DNA (ssDNA and dsDNA, respectively) need to be transfected with the aid of liposomes or specific vectors.[58,59] For example, Wang et al. used natural dsDNA from herring sperm (<50 bp) and a PTEN Gene to synthesize AuNCs in cancer cells by transfection via liposomes for cancer diagnosis.[60] However, the toxicity of cationic liposomes at the site of administration limits their use.[61−63] Hence, we designed the DNRs following our previous study,[64] which could enter cells without the need for liposome transfection or construction of vectors.[65−67] As shown in Figure 1a, DNRs are assembled from several repeated units, each of which is composed of two scaffold strands, S1 and S2, and three staple strands, ST1, ST2 and ST3. In each repeated unit, two different types of 48-base DNA scaffold strands are alternately arranged in an antiparallel manner and are connected by three 32-base folded staple strands (Table S1, Figure S1).

We synthesized the DNRs/AuNCs complex by a simple approach, which involved the incubation of DNRs and $HAuCl_4$ solution with tumor cells. Briefly, the process included three steps: (i) Synthesis of DNRs; (ii) mixing of DNRs with $HAuCl_4$ at 25 °C to produce a mixture of the DNRs and Au^{3+} ions (DNRs/Au^{3+}); and (iii) incubation of the resultant mixture with MCF 7 cells at 37 °C for 1.5 h to obtain DNRs/AuNCs.

In step one, to obtain the DNRs, we mixed the five component DNA strands (1 μM) at a molar ratio of 1:1 in a Tris-Mg^{2+} (40 mM Tris, 20 mM acetic acid, and 10 mM magnesium acetate, pH 7.5) buffer solution, and the mixture was annealed in a PCR machine. The formation of DNRs was confirmed by atomic force microscopy (AFM) (Figure S2). The average width and height of each DNRs were 16.33 ± 1.67 and 1.18 ± 0.15 nm (N = 100), respectively, which are consistent with the theoretical values.[68]

In step two, we incubated 1 μM DNRs with 0.2 mM $HAuCl_4$ at 25 °C in a 1:1 volume ratio to form a mixture of DNRs and Au^{3+} ions (DNRs/Au^{3+}) (Figure 1b). Coordination and chelation complexes may be formed between Au^{3+} and both ring and amino nitrogen of the nucleic acid bases.[69] Therefore, we used DNRs as templates to guide the assembly of gold clusters via DNRs−Au interactions in our study. Dynamic light scattering (DLS) results showed that the zeta potential of $HAuCl_4$ mixed with DNRs was higher than DNRs, demonstrating the formation of DNRs/Au^{3+} (Figure S3).

In step three, we incubated DNRs/Au^{3+} with cancer cells at 37 °C for 1.5 h to obtain DNRs/AuNCs (Figure 1c). Cancer

https://doi.org/10.1021/jacsau.3c00365
JACS Au 2023, 3, 2566−2577

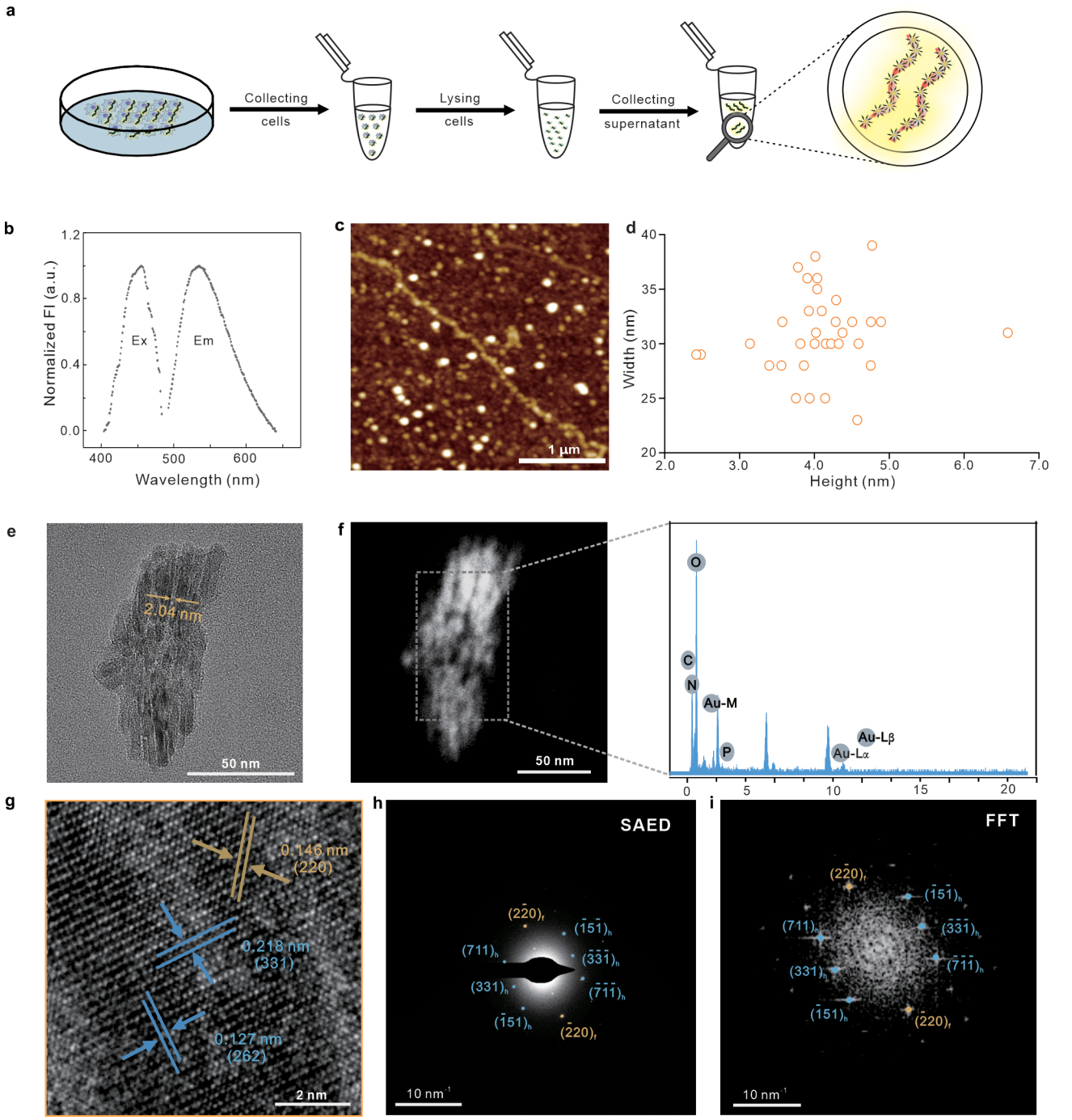

Figure 2. (a) Schematic illustration of the process of extracting DNRs/AuNCs. (b) Fluorescence spectra of DNRs/AuNCs. Excitation wavelength (Ex), emission wavelength (Em). (c) AFM images of DNRs/AuNCs. (d) Statistical distribution of height and width of the DNRs/AuNCs (N = 35). TEM image (e), high-angle darkfield scanning TEM (HAADF-STEM), and energy dispersive X-ray spectroscopy (EDS) energy spectra (f) of DNRs/AuNCs. (g) HRTEM image of DNRs/AuNCs. (h) Selected area electron diffraction (SAED) of DNRs/AuNCs. (i) FFT pattern of DNRs/AuNCs.

cells exhibit a higher amount of glutathione (GSH) and nicotinamide adenine dinucleotide phosphate (NADPH), reactive nitrogen species, and reactive oxygen species (ROS) than those in normal cells, and the unique microenvironment of cancer cells provides an ideal platform for the biosynthesis of DNRs/AuNCs.[70−72] Human breast cancer cells (MCF 7) were adopted as a cancerous cell model, while noncancerous breast cells (MCF 10A) were used as a control. Both MCF 7 and MCF-10A cells were incubated with DNRs/Au^{3+} for 24 h and visualized by using confocal laser scanning microscopy (CLSM) (Figure 1d). The MCF 7 cells displayed bright green fluorescence of the AuNCs, while the signal in the MCF 10A cells was almost indiscernible. This indicates that the AuNCs synthesis is cancer-cell-specific, and it is triggered by upregulated GSH, etc., which reacts with $HAuCl_4$. Given the fact that the different cancerous cells might demonstrate variable levels of GSH expression, we further tested the biosynthesis of AuNCs in human colon cancer HCT 116 cells

https://doi.org/10.1021/jacsau.3c00365
JACS Au 2023, 3, 2566−2577

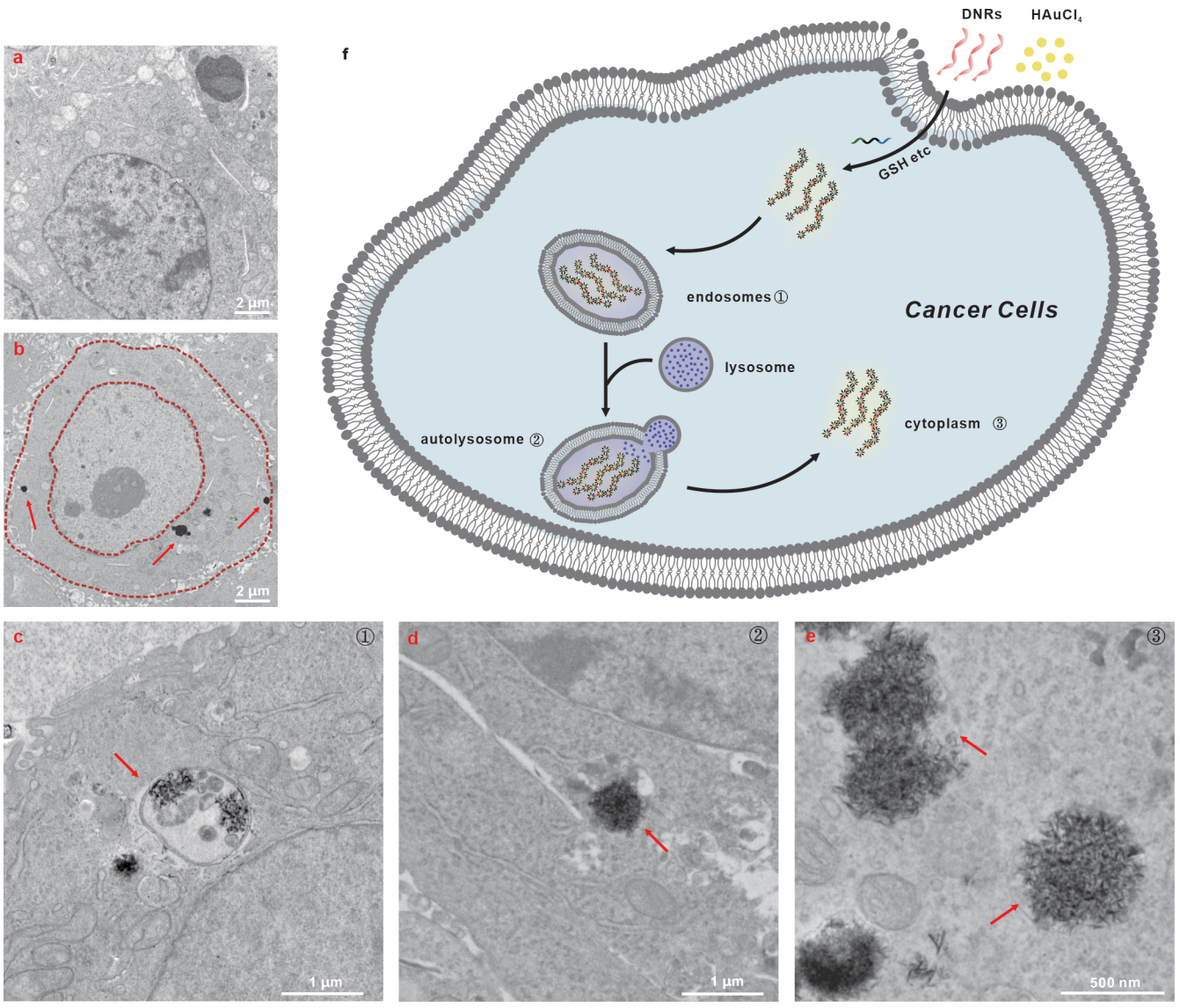

Figure 3. (a) Bio-TEM image of MCF 7 cells. (b) Bio-TEM image of DNRs/Au^{3+}-treated cells. (c) Bio-TEM image of DNRs/AuNCs in endosomes. (d) Bio-TEM image of DNRs/AuNCs in autolysosome. (e) Bio-TEM image of DNRs/AuNCs in cytoplasm. (f) Schematic illustration of different distributions of DNRs/AuNCs in cells.

and human hepatoma Hep G2 cells (Figure S4). In both cases, excellent fluorescence signals were observed in the DNRs/Au^{3+}-treated cells, while such fluorescent characteristics were not observed in the control group (only culture medium) under the same experimental condition. These results indicated that intracellular biosynthesis of AuNCs occurred only at the site of the lesion, enabling the targeted recognition of the tumor.

To verify the successful assembly of AuNCs on the DNRs in live breast cancer cell lines, we conducted a colocalization analysis using Cy5-modified DNRs (Figure 1e). Significant colocalization of the red emission from Cy5-modified DNRs and green emission from the AuNCs was observed after an incubation time of 12 h with a Pearson's correlation coefficient (PCC)[73] of 0.79 (PCC values ranging from −1 to +1). If there is no association between Cy5-modified DNRs and AuNCs, then the expected PCC is 0. A positive PCC means the DNRs and AuNCs are colocalized to some extent; higher values of red are associated with higher values of green. In addition, a negative PCC value indicates that the distributions of the DNRs and AuNCs are inversely related, with higher red values being associated with lower green values, proving that the AuNCs are successfully assembled on the DNRs.

To further confirm the in situ formation of DNRs/AuNCs in the cultured cancer cell lines, we harvested the supernatant of a cellular extract after employing the freeze−thaw cells[74] (a detailed procedure is shown in Figure 2a and provided in the Supporting Information) and characterized this supernatant by its fluorescence spectrum, AFM, transmission electron microscopy (TEM), and X-ray photoelectron spectroscopy (XPS).

The fluorescence spectra of the intracellular biosynthesized DNRs/AuNCs displayed excitation and emission wavelengths at 455 and 530 nm, respectively (Figure 2b). A series of peaks were obtained at 530 nm by irradiating a DNRs/AuNCs solution with different wavelengths of light, as shown in Figure S5, indicating the high uniformity of the biosynthesized DNRs/AuNCs.[75,76] AFM was first used to characterize the biosynthesized DNRs/AuNCs. The average width and height of the DNRs/AuNCs structure was approximately 30.94 and

https://doi.org/10.1021/jacsau.3c00365
JACS Au 2023, 3, 2566−2577

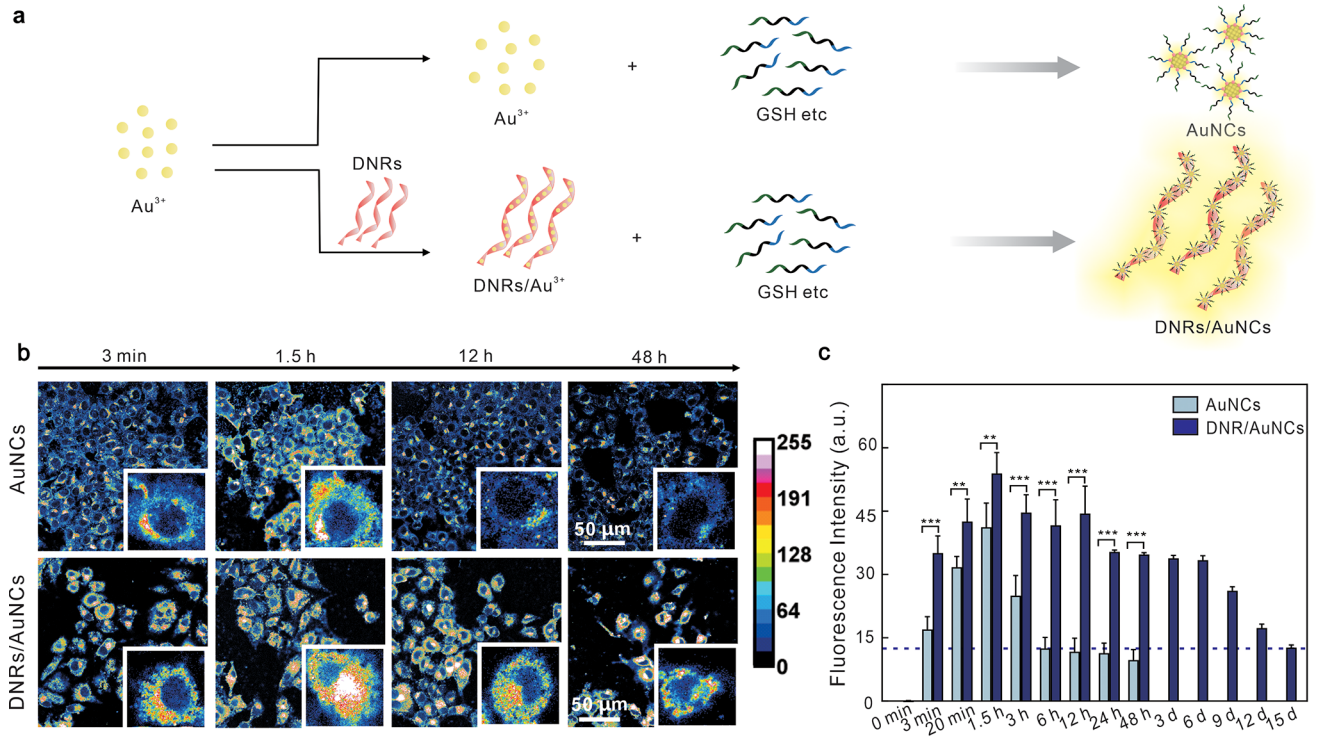

Figure 4. (a) Illustration of the synthesis of AuNCs and DNRs/AuNCs. (b) Laser confocal fluorescence images of $HAuCl_4$, DNRs/Au^{3+} incubated with cells for different times. (c) Fluorescence intensity of $HAuCl_4$ and DNRs/Au^{3+} in cells cultured for different times. The data are presented as the mean ± SD of $n \geq 5$. The asterisk signs (** and ***) are used to indicate $p < 0.05$ and $p < 0.01$, respectively.

4.09 nm (Figure 2c,d); therefore, the diameter of the AuNCs is 2.91 nm, considering the height of the bare DNRs is 1.18 nm. The TEM images demonstrated the formation of a uniform near-monodisperse layered ribbon structure with a mean width of about 2.04 nm (Figure 2e), and energy-dispersive X-ray spectroscopy (EDS) of the areas marked as dashed square proved that the DNRs/AuNCs were composed of Au, P, N, O, and C (Figure 2f), which agrees with the XPS results (Figure S6).

High-resolution TEM of the areas marked as yellow square (Figures 2g and S7) confirmed that the lattice spacing (ca. 1.46 Å) of the intracellular nanoclusters agreed with that of the (220) facet of Au.[77] The lattice spacing (ca. 2.18 and 1.27 Å) matched well with the distance of the adjacent facets (331) and (262) of the Au_2O_3 crystallite.[78] More convincing evidence was provided by the corresponding selected area electron diffraction (SAED) and fast Fourier transform (FFT) results (Figure 2h,i), which confirm the single crystalline nature of DNRs/AuNCs with reflections corresponding to the (220) spacings of Au and the (711), (331), and (151) spacings of Au_2O_3.

To provide additional evidence, we employed bio-TEM for the in situ characterization of the DNRs/AuNCs formation. Figures 3a,b and S8 demonstrate the presence of NCs in MCF 7 cells incubated with DNRs/Au^{3+}, while blank cells or DNRs-treated cells did not show any NCs. TEM images of DNRs/Au^{3+}-treated cells revealed the encapsulation of acicular clusters within endosomes (Figure 3c) or lysosomes (Figure 3d), with some clusters located in the cytoplasm (Figure 3e). Figure 3f illustrates the possible intracellular trafficking of DNRs/AuNCs, where NCs are typically delivered within endosomes that subsequently fuse with lysosomes. A fraction of NCs may escape from lysosomes to the cytoplasm.

To demonstrate the advantages of DNRs nanostructures, we compared DNRs/Au^{3+} treated MCF 7 cells side-by-side with a control group, which was treated with only $HAuCI_4$ (Figure 4a).

To ensure that intracellularly biosynthesized gold NCs exhibit no toxic effect on cells in subsequent experiments, we conducted cytotoxicity tests with different concentrations of the $HAuCl_4$ solution. Figure S9 shows the MTT assay results for cancer cells (MCF 7, Hep G2, and HCT 116) and noncancerous cells (MCF 10A). We can see that the cell survival rate is higher than 60% for all the cells, and the survival rate of the noncancer cells was higher than that of the cancer cells, proving that DNRs/AuNCs and AuNCs are nontoxic to both cancer and noncancer cells. In addition, it was found that the toxicity of the DNRs/AuNCs was lower than that of AuNCs. It has been demonstrated that the AgNCs showed significantly reduced low cytotoxicity even at a high concentration under the protection of the DNA hydrogel.[79] Therefore, our results suggested that DNRs can effectively reduce the cytotoxicity of gold NCs, thereby providing an advantage for long-term tracking experiments.

Next, we performed long-term cell tracking experiments. The fluorescence of both DNRs/AuNCs and AuNCs was observed in the MCF 7 cells at different incubation times by CLSM (Figures 4b and S10). The statistical diagram of the fluorescence intensity is shown in Figure 4c. The fluorescence of the DNRs/AuNCs and AuNCs showed a trend of first increasing and then decreasing over time. The fluorescence intensity was the strongest at 1.5 h for both groups, and the fluorescence intensity of the experimental group (DNRs/AuNCs) was higher than that of the control group (AuNCs) in the range of 3 min to 48 h. The difference was the most significant with the 12 h incubation time (enhancement of ~4

https://doi.org/10.1021/jacsau.3c00365
JACS Au 2023, 3, 2566−2577

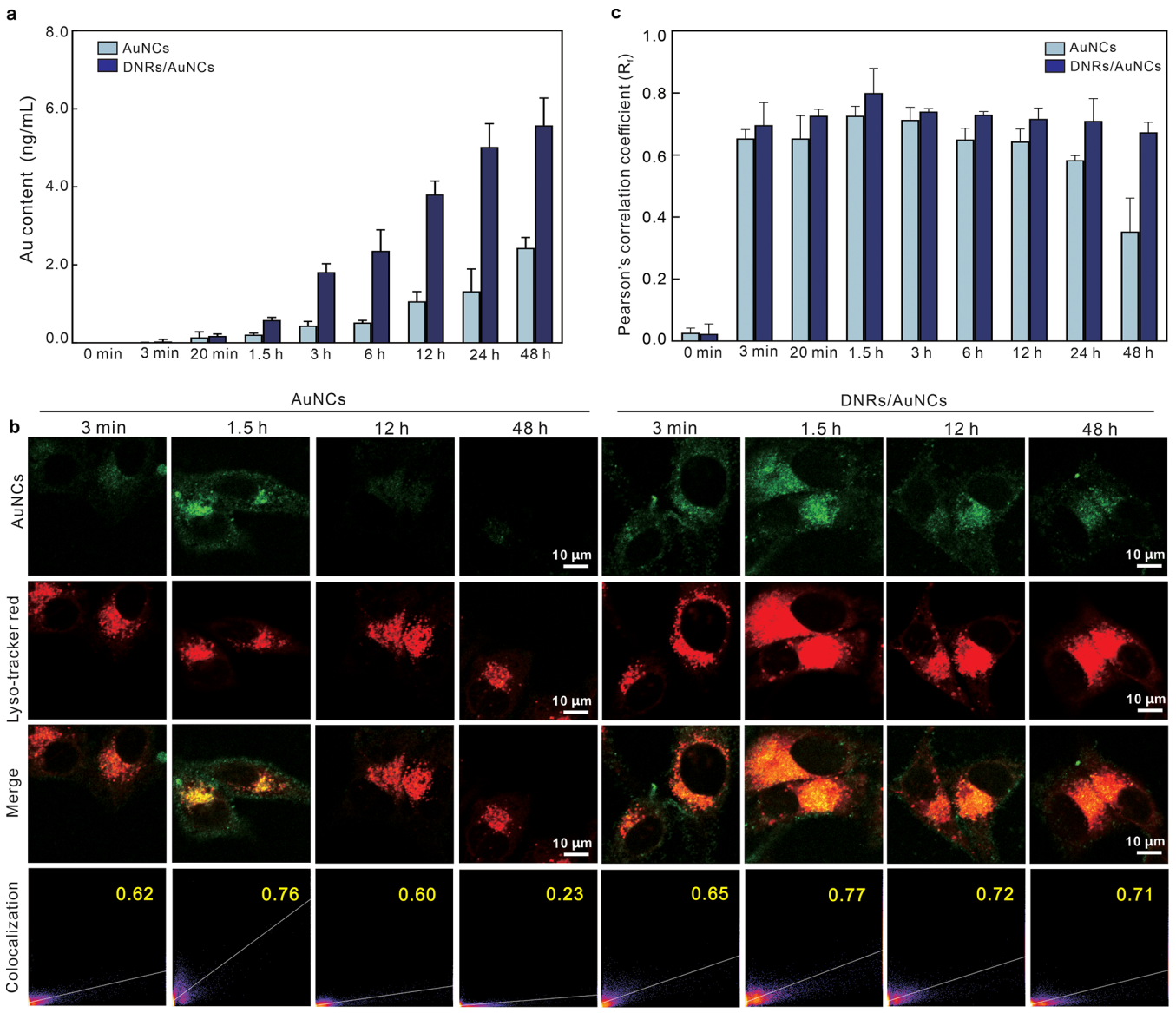

Figure 5. (a) Gold content versus incubation time in DNRs/Au^{3+}-treated cells and $HAuCl_4$ -treated cells. (b) Colocalization analysis between AuNCs (green channel) and Lyso-racker red (red channel). (c) Statistical analysis of colocalization coefficients $HAuCl_4$ and DNRs/Au^{3+} from MCF 7 cells at different time.

times) because, unlike that of the experimental group, the fluorescence intensity of the control group was considerably reduced after the 12 h incubation. With the further increase of incubation time, though progressively declining in intensity, the fluorescence signals of DNRs/Au^{3+} treated MCF 7 cells could still be observed for up to 15 days, which is equal to that of the control group at 6 h of of incubation (enhancement of ~60 times) (Figures 4c and S11). This long-term tracking approach is based on cell proliferation by endogenous nanoprobes rather than the continuous addition of imaging agents during long-term monitoring.[80]

To explore the reasons for the aforementioned phenomenon, we performed ICP-MS to quantify the gold content versus the incubation time. As shown in Figure 5a, the gold content of the experimental group was higher than that of the control group at all time points, indicating that DNRs is more conducive to the intracellular biosynthesis of AuNCs, which led to the higher fluorescence intensity of DNRs/AuNCs. However, when incubated for 48 h, the fluorescence intensity of DNRs/AuNCs was 3.6 times that of AuNCs, but the gold content of DNRs/AuNCs was only 2.3 times that of AuNCs, which implied that there might be another factor influencing the fluorescence intensity of AuNCs. Unexpectedly, the intracellular gold content of both DNRs/AuNCs and AuNCs showed an increasing trend within the time frame of 48 h, while the fluorescence intensity decreased after 1.5 h of incubation, suggesting that the evacuation of AuNCs from the cells was not the reason for the decrease in fluorescence intensity.

We further used a fluorescence colocalization technique to study the subcellular localization of fluorescent gold clusters in MCF 7 cells (Figures 5b,c and S12). Pearson's correlation coefficient was used for quantification of the colocalization of the red emission from the Lyso-tracker red (a commercial dye for visualizing lysosome) and green emission from AuNCs. The results showed that the Pearson's correlation coefficient of both the experimental group and the control group increased in the 0−1.5 h range and began to decrease after 1.5 h, which

https://doi.org/10.1021/jacsau.3c00365
JACS Au 2023, 3, 2566−2577

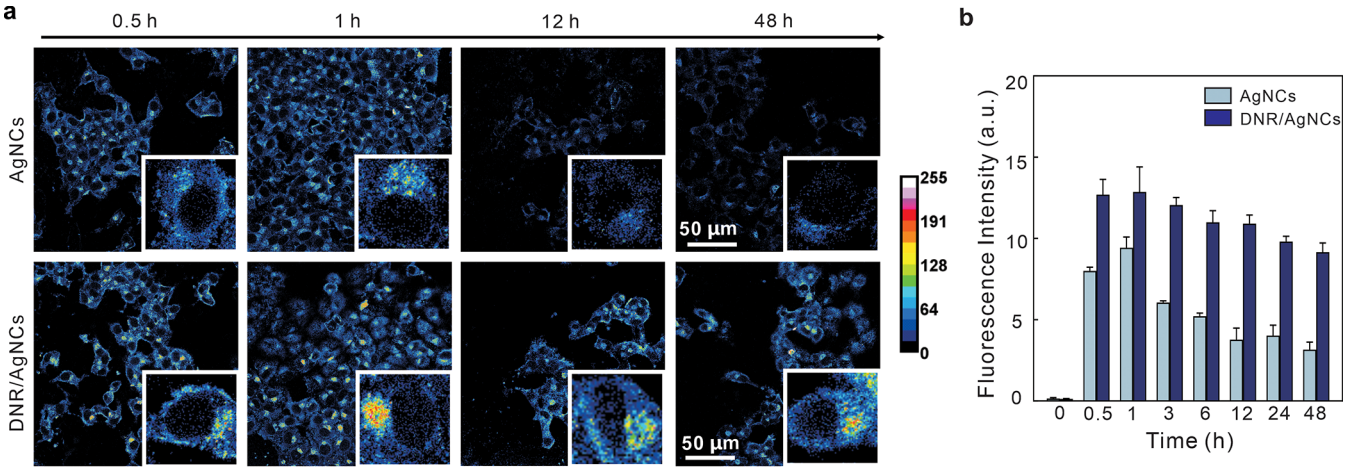

Figure 6. (a) Laser confocal images of MCF 7 cells incubated with DNRs/Ag^+ or $AgNO_3$ for different times. (b) Fluorescence intensity of $AgNO_3$ and DNRs/Ag^+ in cells cultured for different times.

was consistent with the observed trend of fluorescence intensity. Based on our observations, we hypothesized that the initial increase in fluorescence was a result of cluster aggregation in lysosomes, which has been observed previously for AuNPs formed into self-assembled nanostructures using chitosan.[81] Subsequently, the decrease in fluorescence could be attributed to the degradation of gold clusters within the lysosomes. A previous study has demonstrated that ROS generated by NADPH oxidase inside lysosomes can induce damage to gold nanoparticles.[82] After 48 h of incubation, the control group exhibited a significant decrease in Pearson's correlation coefficient, reaching only half of the maximum value. In contrast, the experimental group showed a mere 6% decline in the colocalization rate. This suggests that DNRs enhance the stability of AuNCs within lysosomes, which could explain the stronger fluorescence exhibited by DNRs/AuNCs after an extended incubation period.

To verify the universality of this method, we attempted to synthesize other types of metal NCs using a DNR-assisted technique. The nucleic acid bases have been found to form coordination with many metal ions, such as silver (Ag).[83] Thus, we synthesized DNRs/AgNCs by the same approach, and more details about the preparation and characterization of the AgNCs are given in the Supporting Information (Figures S13–S17). Similarly, cells treated with only $AgNO_3$ were used as a control. We observed that the fluorescence of the DNRs/Ag^+-treated MCF 7 cells was higher than that of the cells treated with only $AgNO_3$. After 48 h of incubation, the experimental group still demonstrated strong fluorescence, whereas no fluorescence was observed in the control group (Figures 6 and S18). These results suggested that the DNR-assisted biosynthesis of metal NCs could be used as a potential technique for clinical oncology diagnosis.

CONCLUSIONS

In the current study, we showed that DNR-assisted intracellular biosynthesis of metal NCs is a general strategy by which we can efficiently synthesize brighter and more stable fluorescent metal NCs for cancer cell imaging. This strategy uses DNRs as a template for the assembly of metal NCs in cancer cells, which showed stronger intracellular fluorescence than that of those treated with preionic solutions alone owing to the higher synthesis efficiency and stability of metal NCs in the lysosome. Finally, the potential application of DNRs/AuNCs as fluorescent probes for the long-term tracking of cancer cells was demonstrated. It is to be noted that this fluorescence could be maintained for up to 15 days without the continuous addition of imaging agents during long-term monitoring, which exhibit an ∼60× enhancement of tracking time compared to free AuNCs. This study suggests that the DNRs-assisted intracellular biosynthesis of metal NCs could be used as a potential fluorescent technique for long-term cellular tracking and real-time observation of dynamic cell migration, division, and lysis, which will considerably facilitate the early diagnosis of cancer.

MATERIALS AND METHODS

Materials and Instruments

Dulbecco's modified Eagle's medium/Nutrient Mixture F-12 (DMEM/F12), hydrocortisone, insulin, nonessential amino acid (NEAA), epidermal growth factor (EGF), horse serum (HS) and 3-(4,5)-dimethylthiahiazo(-z-y1)-3,5-diphenytetrazoliumromide (MTT) were purchased from Procell Life Science&Technology Co.. Dimethyl sulfoxide, Dulbecco's modified Eagle's medium (DMEM), trypsin-EDTA solution, penicillin-streptomycin, and fetal bovine serum (FBS) were purchased from Sangon Biotech (Shanghai). Choloroauric acid ($HAuCl_4$), silver nitrate ($AgNO_3$), tris-(hydroxymethyl) methyl aminomethane THAM (Tris), magnesium acetate ($MgAc_2$), and nitric acid (HNO_3) were purchased from Aladdin. All DNA strands were synthesized from Sangon Biotech (Shanghai). These DNA oligonucleotides were purified by high-performance liquid chromatography (HPLC, purity > 95%) and suspended in double distilled water (Shanghai Sangon) to give a final concentration of 100 μM. Fluorescence spectra were recorded on a F-4500 spectrometer (Hitich, Japan). AFM images were collected on a MultiMode 8 atomic force microscope with a NanoScope V Controller (Bruker, Inc.). TEM images were recorded on an FEI Talos F200X microscope operating at 200 kV. X-ray photoelectron spectroscopy was performed on a Thermo Scientific K-Alpha+ X-ray photoelectron spectrometer. X-ray powder diffraction was performed on a BrukerD 8 ADVANCE X-ray powder diffractometer. Laser confocal maps were recorded on an N-SIMS (Nikon, Japan) laser confocal microscope. Inductively coupled plasma mass spectrometry (ICP-MS) was recorded on an Agilent 7800 ICP-MS instrument. Bioelectron micrographs were recorded on a Hitachi H-7650 Biotransmission Electron Microscope. Cytotoxicity was recorded on a Synergy H1 enzyme-labeled instrument.

https://doi.org/10.1021/jacsau.3c00365
JACS Au 2023, 3, 2566–2577

Synthesis of the DNRs

All the staple strands, the scaffold strands (in the molar ratio of 1:1), and magnesium acetate (10 mM) were mixed to a volume of 50 μL in Tris-HAc buffer consisting of 40 mM Tris (pH 7.5) and 20 mM acetic acid. Successful folding of the DNRs was observed at the following conditions: subjecting the mixture to thermal annealing by heating to 85 °C followed by slow cooling to 25 °C for about 2 h. Then the DNRs was purified using Microcon centrifugal filter devices (100 kDa MWCO, 3000*g* speed, 10 min, 3 times) followed by washing with the buffer (40 mM Tris-HAc, 10 mM Mg^{2+}, pH 7.5) to remove single stranded DNA after assembly. The concentration of the DNRs after purification (C_{after}) could be calculated from the absorbance of the DNRs before (A_{before}) and after (A_{after}) the purification (C_{after}) by the following equation:

$$C_{after} = \frac{A_{after}}{A_{before}} \times C_{before} \quad (1)$$

We use the concentration of one copy unit to represent the concentration of the DNRs in this report. The concentration of copy units before purification (C_{before}) was assumed equal to the scaffold DNA concentration quantified by measuring the OD260 with the extinction coefficient ε260 calculated with Sangon Biotech's Oligo Analyzer.

Biosynthesis of the AuNCs

Gold nanoclusters were biosynthesized in situ through incubation with 50 μL of $HAuCl_4$ (0.2 mM) and 50 μL of buffer (Tris-Mg^{2+}, pH 7.5) under 37 °C and 5% CO_2 for different times.

Biosynthesis of the DNRs/AuNCs

First, these cells were incubated in a Petri dish and cultured at 37 °C and 5% CO_2 for 24 h. Then, 1 μM DNRs was incubated with 0.2 mM $HAuCl_4$ at room temperature in a 1:1 volume ratio to form a mixture of DNRs and metal ion (DNRs/Au^{3+}), DNRs/Au^{3+} were added to the culture dishes and incubated with the cells for different times, and finally DNRs/AuNCs were obtained.

Biosynthesis of the AgNCs

Silver nanoclusters were biosynthesized in situ through incubation with 50 μL of $AgNO_3$ (34 μg/mL) and 50 μL of buffer (Tris-Mg^{2+}, pH 7.5) under 37 °C and 5% CO_2 for different time.

Biosynthesis of the DNRs/AgNCs

First, these cells were incubated in a Petri dish and cultured at 37 °C and 5% CO_2 for 24 h. Then, 1 μM DNRs was incubated with 34 μg/mL $AgNO_3$ at room temperature in a 1:1 volume ratio to form a mixture of DNRs and metal ion (DNRs/Ag^{+}), DNRs/Ag^{+} was added to the culture dishes and incubated with the cells for different times, and finally DNRs/AgNCs were obtained.

Cell Culture

Hep G2, human liver cancer cells, MCF 7, human breast cancer cells, and HCT 116, human colon cancer cells, were grown in DMEM supplemented with 10% FBS and 1% Pen Strep Glutamine (Gibco) in 5% CO_2 incubator at 37 °C. The human normal breast cell line, MCF 10A, was purchased from Procell Life Science&Technology Co, Ltd. and grown in DMEM/F12 medium supplemented with 5% HS, 20 ng/mL EGF, 0.5 ug/mL hydrocortisone, 10 ug/mL insulin, 1% nonessential amino acids (NEAA), and 1% 100× penicillin-streptomycin solution (P/S) in 5% CO_2 incubator at 37 °C. The culture medium was changed every 2 days, and when the density of cells reached 70−80%, the cells were digested with trypsinization for the experiments.

Characterization of DNRs/AuNCs

First, MCF 7 cells were incubated with $HAuCl_4$ and DNRs for 24 h, and then the cells were lysed by repeated freeze−thaw methods (3 cycles of freezing for 15 s and thawing for 75 s) with liquid nitrogen (−196 °C) and a water bath (37 °C) for cell lysis, and then the lysed tissue solution was centrifuged 8000 rpm for 20 min. The supernatant containing the biosynthesized nanoclusters was collected for further characterization. The biosynthesized DNRs/AuNCs were characterized by fluorescence spectra, XPS, AFM, and TEM.

XPS. First, the supernatant from the lysed cells was placed in a centrifuge tube, and then the tube was placed in a freezer bottle and frozen for 4 h at −60 °C. Finally, the frozen samples were processed overnight in a freeze-dryer to obtain frozen powder samples. The samples were then examined on a BrukerD 8 ADVANCE powder X-ray diffractometer and a Thermo Scientific K-Alpha+ X-ray photoelectron spectrometer.

AFM. A 3 μL amount of the cell lysate (DNRs/AuNCs) and DNRs (1 μM) was deposited on fresh mica sheets and allowed to adsorb on the surface for 2 min. They were eventually scanned under tapping mode on a MultiMode 8 AFM with a NanoScope V Controller (Bruker, Inc.).

TEM. A volume of 10 μL of cell lysate was deposited on a copper grid for 30 min, dried, and then scanned using a FEI Talos F200X machine.

Bio-TEM. Cells cultured in DMEM were used as control, 0.2 mM $HAuCl_4$ solution alone with cells for 12 h, 1 μM DNRs solution alone with cells for 24 h, and the cells were incubated with 0.2 mM $HAuCl_4$ solution and 1 μM DNRs solution for 24 h. The cells above 10^6 were then digested with trypsin and centrifuged at 3000 rpm for 10 min, and 2−3 rice-like samples were collected from the bottom of the tube, and the supernatant was finally discarded, and prechilled 25% glutaraldehyde fixative was slowly added along the wall of the tube and stored at 4 °C for 12 h. It was then observed under a biological transmission electron microscope.

Characterization of DNRs/AgNCs

The same method for characterization was used as DNRs/AuNCs.

Cellular Imaging

HCT 116, Hep G2, MCF 7, and MCF 10A cells were seeded on 15 mm confocal Petri dishes. Then a concentration of 0.2 mM $HAuCl_4$ and 1 μM DNRs was incubated with the cells for 24 h. Finally, the cells were washed with PBS for 3 times and the fluorescence was observed under a confocal laser microscope. (N-SIMS). Each experiment is repeated three times.

The MCF 7 cells were seeded in 15 mm confocal Petri dishes. Then the concentration of 34 μg/mL $AgNO_3$ and 1 μM DNRs was incubated with the cells for 24 h. Finally, the cells were washed with PBS for 3 times and the fluorescence was observed under a confocal laser microscope. (N-SIMS). Each experiment is repeated three times.

Cell Cytotoxicity Assay

HCT 116, Hep G2, MCF 7 and MCF 10A cells (1×10^4 cells per well) were seeded in 96-well enzyme label plates and cultured for 24 h in a humid atmosphere with 5% CO_2 at 37 °C. After removing the old medium and adding DMEM containing different concentrations of $HAuCl_4$, DNRs/Au^{3+} (concentration of DNRs added was 1 μM, concentrations of $HAuCl_4$ were 0, 0.05, 0.1, 0.2, 0.4, 0.6, 0.8, 1, 1.5, 2 mM) were incubated with the cells for 24 h. Then, 20 μL of MTT solution (5 mg/mL) was added to each well and incubated for 4 h. Next, 200 μL of DMSO was added to each well and oscillated for 10 min to allow the crystal to be fully dissolved. Finally, Absorbance was measured at a wavelength of 490 nm. (Cells incubated with DMEM were used as controls). The cytotoxicity of AuNCs and DNRs/AuNCs was calculated according to eq 2:

$$\text{cell viability} = \frac{A_{test}}{A_{control}} \times 100\% \quad (2)$$

A_{test} is mean of Abs value of test group, and $A_{control}$ is the mean Abs value of control.

Quantification of Intracellular Gold Content

MCF 7 cells were seeded at a density of 1×10^5 in 6-well plates. After 24 h, $HAuCl_4$ and DNRs/Au^{3+} were incubated with cells for 0, 30 min, 1.5 3, 6, 12, 24, and 48 h. The old medium was poured off and washed three times with PBS to remove uninternalized AuNCs and DNRs/AuNCs. Then cells were digested by adding trypsin-EDTA (0.05% trypsin-EDTA) to digest the cells and count the cells. The

https://doi.org/10.1021/jacsau.3c00365
JACS Au 2023, 3, 2566−2577

collected cells were completely lysed in 3 mL of aqua regia for 24 h. Then samples were heated at 120 °C in an oil bath until the aqua regia evaporated completely and finally dispersed in 5 mL of 2% HNO_3 for ICP-MS measurements.

Long-Term Cellular Tracing

MCF 7 cells in a logarithmic growth phase were seeded in an ordinary Petri dish and 15 mm confocal Petri dish at a density of 1×10^5 cells/well and incubated in DMEM for 24 h. Then the old medium in the 15 mm confocal dishes was replaced with 1 mL of DMEM containing 50 μL of $HAuCl_4$ (0.2 mM) and 50 μL of DNRs (5 μM), and incubated for 24 h at 37 °C (day 0). Then the cells were diluted and subcultured in an ordinary Petri dish for 0−15 days regeneration, while the cells in the confocal dish were used for confocal imaging. These processes are repeated until the sixth generation.

■ ASSOCIATED CONTENT

Supporting Information

The Supporting Information is available free of charge at https://pubs.acs.org/doi/10.1021/jacsau.3c00365.

Additional experimental results of the studied samples, including DNA sequences, DLS, AFM, fluorescence spectra, XPS, TEM, EDS, cytotoxicity assay, and confocal image analysis (PDF)

■ AUTHOR INFORMATION

Corresponding Authors

Xiangyuan Ouyang − *Xi'an Key Laboratory of Functional Supramolecular Structure and Materials, Key Laboratory of Synthetic and Natural Functional Molecule of Ministry of Education, College of Chemistry & Materials Science, Northwest University, Xi'an, Shaanxi 710127, P. R. China*; orcid.org/0000-0003-4263-7694; Email: ouyangxy@nwu.edu.cn

Huaiyu Bu − *Key Laboratory of Resource Biology and Biotechnology in Western China (Ministry of Education), College of Life Sciences, Northwest University, Xi'an, Shaanxi 710069, PR China*; Email: buhy@nwu.edu.cn

Ying Wan − *School of Mechanical Engineering, Nanjing University of Science and Technology, Nanjing 210094, China*; Email: wanying@njust.edu.cn

Authors

Nan Jia − *Xi'an Key Laboratory of Functional Supramolecular Structure and Materials, Key Laboratory of Synthetic and Natural Functional Molecule of Ministry of Education, College of Chemistry & Materials Science, Northwest University, Xi'an, Shaanxi 710127, P. R. China*

Jing Luo − *Key Laboratory of Resource Biology and Biotechnology in Western China (Ministry of Education), College of Life Sciences, Northwest University, Xi'an, Shaanxi 710069, PR China*

Le Li − *Xi'an Key Laboratory of Functional Supramolecular Structure and Materials, Key Laboratory of Synthetic and Natural Functional Molecule of Ministry of Education, College of Chemistry & Materials Science, Northwest University, Xi'an, Shaanxi 710127, P. R. China*

Jiangshan Xue − *Key Laboratory of Resource Biology and Biotechnology in Western China (Ministry of Education), College of Life Sciences, Northwest University, Xi'an, Shaanxi 710069, PR China*

Gang Xie − *Xi'an Key Laboratory of Functional Supramolecular Structure and Materials, Key Laboratory of Synthetic and Natural Functional Molecule of Ministry of Education, College of Chemistry & Materials Science, Northwest University, Xi'an, Shaanxi 710127, P. R. China*

Complete contact information is available at: https://pubs.acs.org/10.1021/jacsau.3c00365

Author Contributions

‖X. Ouyang, N. Jia, J. Luo, and L. Li, contributed equally to this work. The manuscript was written through contributions of all authors.

Notes

The authors declare no competing financial interest.

■ ACKNOWLEDGMENTS

This work is supported by grants 21605124 and 21973074 from the National Natural Science Foundation of China, the Young Talent Fund of University Association for Science and Technology in Shaanxi, China (20180603), 2022JZ-08 from The Natural Science Foundation of Shaanxi Province, the China Postdoctoral Science Foundation Funded Project (2019M650270, 2021T140556), the Open Fund of Key Laboratory of Synthetic and Natural Functional Molecules, Ministry of Education (KLSNFM2020009), the "Top-rated Discipline" construction scheme of Shaanxi higher education and "Tang scholar".

■ REFERENCES

(1) Samanta, S.; Gong, W. J.; Li, W.; Sharma, A.; Shim, I.; Zhang, W.; Das, P. T.; Pan, W. H.; Liu, L. W.; Yang, Z. G.; et al. Organic fluorescent probes for stochastic optical reconstruction microscopy (STORM): Recent highlights and future possibilities. *Coord. Chem. Rev.* **2019**, *380*, 17−34.

(2) Feng, Y. N.; Das, P. J.; Young, R. M.; Brown, P. J.; Hornick, J. E.; Weber, J. A.; Seale, J. S.; Stern, C. L.; Wasielewski, M. R.; Stoddart, J. F. Alkoxy-Substituted Quadrupolar Fluorescent Dyes. *J. Am. Chem. Soc.* **2022**, *144*, 16841−16854.

(3) Lei, Z. H.; Sun, C. X.; Pei, P.; Wang, S. F.; Li, D. D.; Zhang, X.; Zhang, F. Stable, wavelength-tunable fluorescent dyes in the NIR-II region for in vivo high-contrast bioimaging and multiplexed biosensing. *Angew. Chem., Int. Ed.* **2019**, *131*, 8250−8255.

(4) García de Arquer, F. P.; Talapin, D. V.; Klimov, V. I.; Arakawa, Y.; Bayer, M.; Sargent, E. H. Semiconductor quantum dots: Technological progress and future challenges. *Science* **2021**, *373*, No. eaaz8541.

(5) McHugh, K. J.; Jing, L. H.; Behrens, A. M.; Jayawardena, S.; Tang, W.; Gao, M. Y.; Langer, R.; Jaklenec, A. Biocompatible semiconductor quantum dots as cancer imaging agents. *Adv. Mater.* **2018**, *30*, 1706356.

(6) Mueller, S.; Lüttig, J.; Brenneis, L.; Oron, D.; Brixner, T. Observing multiexciton correlations in colloidal semiconductor quantum dots via multiple-quantum two-dimensional fluorescence spectroscopy. *ACS Nano* **2021**, *15*, 4647−4657.

(7) Wu, J. H.; Zaccara, S.; Khuperkar, D.; Kim, H.; Tanenbaum, M. E.; Jaffrey, S. R. Live imaging of mRNA using RNA-stabilized fluorogenic proteins. *Nat. Methods.* **2019**, *16*, 862−865.

(8) Wang, M. J.; Da, Y. F.; Tian, Y. Fluorescent proteins and genetically encoded biosensors. *Chem. Soc. Rev.* **2023**, *52*, 1189−1214.

(9) Hirano, M.; Ando, R.; Shimozono, S.; Sugiyama, M.; Takeda, N.; Kurokawa, H.; Deguchi, R.; Endo, K.; Haga, K.; Takai-Todaka, R.; et al. A highly photostable and bright green fluorescent protein. *Nat. Biotechnol.* **2022**, *40*, 1132−1142.

(10) Chang, J.; Romei, M. G.; Boxer, S. G. Structural evidence of photoisomerization pathways in fluorescent proteins. *J. Am. Chem. Soc.* **2019**, *141*, 15504−15508.

(11) Hao, C. L.; Wu, X. L.; Sun, M. Z.; Zhang, H. Y.; Yuan, A. M.; Xu, L. G.; Xu, C. L.; Kuang, H. Chiral core-shell upconversion nanoparticle@ MOF nanoassemblies for quantification and bioimaging of reactive oxygen species in vivo. *J. Am. Chem. Soc.* **2019**, *141*, 19373−19378.
(12) Li, Z. H.; Yuan, H.; Yuan, W.; Su, Q. Q.; Li, F. Y. Upconversion nanoprobes for biodetections. *Coord. Chem. Rev.* **2018**, *354*, 155−168.
(13) Chen, H.; Ding, B.; Ma, P.; Lin, J. Recent progress in upconversion nanomaterials for emerging optical biological applications. *Adv. Drug Delivery Rev.* **2022**, *188*, 114414.
(14) Abdelfattah, A. S.; Kawashima, T.; Singh, A.; Novak, O.; Liu, H.; Shuai, Y. C.; Huang, Y. C.; Campagnola, L.; Seeman, S. C.; Yu, J. N.; et al. Bright and photostable chemigenetic indicators for extended in vivo voltage imaging. *Science* **2019**, *365*, 699−704.
(15) Li, H. D.; Kim, D.; Yao, Q. C.; Ge, H. Y.; Chung, J.; Fan, J. L.; Wang, J. Y.; Peng, X. J.; Yoon, J. Activity-based NIR enzyme fluorescent probes for the diagnosis of tumors and image-guided surgery. *Angew. Chem., Int. Ed.* **2021**, *133*, 17408−17429.
(16) Gao, L. Q.; Wang, W.; Wang, X.; Yang, F.; Xie, L. X.; Shen, J.; Brimble, M. A.; Xiao, Q. C.; Yao, S. Q. Fluorescent probes for bioimaging of potential biomarkers in Parkinson's disease. *Chem. Soc. Rev.* **2021**, *50*, 1219−1250.
(17) Cezan, S. D.; Nalbant, A. A.; Buyuktemiz, M.; Dede, Y.; Baytekin, H. T.; Baytekin, B. Control of triboelectric charges on common polymers by photoexcitation of organic dyes. *Nat. Commun.* **2019**, *10*, 276.
(18) Li, K.; Ren, T. B.; Huan, S. Y.; Yuan, L.; Zhang, X. B. Progress and perspective of solid-state organic fluorophores for biomedical applications. *J. Am. Chem. Soc.* **2021**, *143*, 21143−21160.
(19) Filali, S.; Pirot, F.; Miossec, P. Biological applications and toxicity minimization of semiconductor quantum dots. *Trends Biotechnol.* **2020**, *38*, 163−177.
(20) Li, J. J.; Li, B.; Sun, J.; Ma, C.; Wan, S. K.; Li, Y. X.; Göstl, R.; Herrmann, A.; Liu, K.; Zhang, H. J. Engineered Near-Infrared Fluorescent Protein Assemblies for Robust Bioimaging and Therapeutic Applications. *Adv. Mater.* **2020**, *32*, 2000964.
(21) Loo, J. F. C.; Chien, Y. H.; Yin, F.; Kong, S. K.; Ho, H. P.; Yong, K. T. Upconversion and downconversion nanoparticles for biophotonics and nanomedicine. *Coord. Chem. Rev.* **2019**, *400*, 213042.
(22) Lin, Z. K.; Goswami, N.; Xue, T. T.; Chai, O. J. H.; Xu, H. J.; Liu, Y. X.; Su, Y.; Xie, J. P. Engineering metal nanoclusters for targeted therapeutics: from targeting strategies to therapeutic applications. *Adv. Funct. Mater.* **2021**, *31*, 2105662.
(23) Kim, J. S.; Chang, H.; Kang, S. S.; Cha, S.; Cho, H.; Kwak, S. J.; Park, N.; Kim, Y.; Kang, D.; Song, C. K.; et al. Critical roles of metal-ligand complexes in the controlled synthesis of various metal nanoclusters. *Nat. Commun.* **2023**, *14*, 3201.
(24) Liu, Z. H.; Wu, Z. N.; Yao, Q. F.; Cao, Y. T.; Chai, O. J. H.; Xie, J. P. Correlations between the fundamentals and applications of ultrasmall metal nanoclusters: Recent advances in catalysis and biomedical applications. *Nano Today* **2021**, *36*, 101053.
(25) Chen, Z. X.; Chen, M.; Cheng, Y. F.; Kowada, T.; Xie, J. H.; Zheng, X. C.; Rao, J. H. Exploring the condensation reaction between aromatic nitriles and amino thiols to optimize in situ nanoparticle formation for the imaging of proteases and glycosidases in cells. *Angew. Chem., Int. Ed.* **2020**, *59*, 3272−3279.
(26) Gao, F. P.; Cai, P. J.; Yang, W. J.; Xue, J. Q.; Gao, L.; Liu, R.; Wang, Y. L.; Zhao, Y. W.; He, X.; Zhao, L. N.; et al. Ultrasmall [^{64}Cu] Cu nanoclusters for targeting orthotopic lung tumors using accurate positron emission tomography imaging. *ACS Nano* **2015**, *9*, 4976−4986.
(27) Du, T. Y.; Zhao, C. Q.; ur Rehman, F. U.; Lai, L. M.; Li, X. Q.; Sun, Y.; Luo, S. H.; Jiang, H.; Gu, N.; Selke, M.; et al. In Situ Multimodality Imaging of Cancerous Cells Based on a Selective Performance of Fe^{2+}-Adsorbed Zeolitic Imidazolate Framework-8. *Adv. Funct. Mater.* **2017**, *27*, 1603926.
(28) Lai, L. M.; Zhao, C. Q.; Su, M. N.; Ye, J.; Jiang, H.; Wang, X. M. In vivo rapid fluorescence imaging of Alzheimer's disease through accurate target bio-marking of zinc gluconate. *Sci. Bull.* **2015**, *60*, 1465−1467.
(29) Kang, X.; Li, Y. W.; Zhu, M. Z.; Jin, R. C. Atomically precise alloy nanoclusters: syntheses, structures, and properties. *Chem. Soc. Rev.* **2020**, *49*, 6443−6514.
(30) West, A. L.; Schaeublin, N. M.; Griep, M. H.; Maurer-Gardner, E. I.; Cole, D. P.; Fakner, A. M.; Hussain, S. M.; Karna, S. P. In situ synthesis of fluorescent gold nanoclusters by nontumorigenic microglial cells. *ACS Appl. Mater. Interfaces.* **2016**, *8*, 21221−21227.
(31) Jin, H.; Heller, D. A.; Sharma, R.; Strano, M. S. Size-dependent cellular uptake and expulsion of single-walled carbon nanotubes: single particle tracking and a generic uptake model for nanoparticles. *ACS Nano* **2009**, *3*, 149−158.
(32) Taylor, A.; Wilson, K. M.; Murray, P.; Fernig, D. G.; Levy, R. Long-term tracking of cells using inorganic nanoparticles as contrast agents: are we there yet? *Chem. Soc. Rev.* **2012**, *41*, 2707−2717.
(33) Wang, Z. K.; Chen, S. J.; Lam, J. W.; Qin, W.; Kwok, R. T.; Xie, N.; Hu, Q. L.; Tang, B. Z. Long-term fluorescent cellular tracing by the aggregates of AIE bioconjugates. *J. Am. Chem. Soc.* **2013**, *135*, 8238−8245.
(34) Liu, H. W.; Li, K.; Hu, X. X.; Zhu, L. M.; Rong, Q. M.; Liu, Y. C.; Zhang, X. B.; Hasserodt, J.; Qu, F. L.; Tan, W. H. In situ localization of enzyme activity in live cells by a molecular probe releasing a precipitating fluorochrome. *Angew. Chem., Int. Ed.* **2017**, *56*, 11788−11792.
(35) Li, K.; Hu, X. X.; Liu, H. W.; Xu, S.; Huan, S. Y.; Li, J. B.; Deng, T. G.; Zhang, X. B. In situ imaging of furin activity with a highly stable probe by releasing of precipitating fluorochrome. *Anal. Chem.* **2018**, *90*, 11680−11687.
(36) Pu, K. Y.; Shuhendler, A. J.; Jokerst, J. V.; Mei, J. G.; Gambhir, S. S.; Bao, Z. N.; Rao, J. H. Semiconducting polymer nanoparticles as photoacoustic molecular imaging probes in living mice. *Nat. Nanotechnol.* **2014**, *9*, 233−239.
(37) Gu, K. Z.; Qiu, W. S.; Guo, Z. Q.; Yan, C. X.; Zhu, S. Q.; Yao, D. F.; Shi, P.; Tian, H.; Zhu, W. H. An enzyme-activatable probe liberating AIEgens: on-site sensing and long-term tracking of β-galactosidase in ovarian cancer cells. *Chem. Sci.* **2019**, *10*, 398−405.
(38) Hou, W. X.; Xia, F. F.; Alfranca, G.; Yan, H.; Zhi, X.; Liu, Y. L.; Peng, C.; Zhang, C. L.; de la Fuente, J. M. D.; Cui, D. X. Nanoparticles for multi-modality cancer diagnosis: simple protocol for self-assembly of gold nanoclusters mediated by gadolinium ions. *Biomaterials* **2017**, *120*, 103−114.
(39) Nam, J.; Won, N.; Jin, H.; Chung, H.; Kim, S. pH-induced aggregation of gold nanoparticles for photothermal cancer therapy. *J. Am. Chem. Soc.* **2009**, *131*, 13639−13645.
(40) Wu, Z. N.; Du, Y. N.; Liu, J. L.; Yao, Q. F.; Chen, T. K.; Cao, Y. T.; Zhang, H.; Xie, J. P. Aurophilic interactions in the self-assembly of gold nanoclusters into nanoribbons with enhanced luminescence. *Angew. Chem., Int. Ed.* **2019**, *58*, 8139−8144.
(41) Xia, F. F.; He, A.; Zhao, H. T.; Sun, Y.; Duan, Q.; Abbas, S. J.; Liu, J. J.; Xiao, Z. Y.; Tan, W. H. Molecular engineering of aptamer self-assemblies increases in vivo stability and targeted recognition. *ACS Nano* **2022**, *16*, 169−179.
(42) Wu, Z. N.; Liu, J. L.; Gao, Y.; Liu, H. W.; Li, T. T.; Zou, H. Y.; Wang, Z. G.; Zhang, K.; Wang, Y.; Zhang, H.; et al. Assembly-induced enhancement of Cu nanoclusters luminescence with mechanochromic property. *J. Am. Chem. Soc.* **2015**, *137*, 12906−12913.
(43) Yahia-Ammar, A.; Sierra, D.; Merola, F.; Hildebrandt, N.; Le Guével, X. L. Self-assembled gold nanoclusters for bright fluorescence imaging and enhanced drug delivery. *ACS Nano* **2016**, *10*, 2591−2599.
(44) Chen, L. J.; Ren, Y. Y.; Wu, N. W.; Sun, B.; Ma, J. Q.; Zhang, L.; Tan, H. W.; Liu, M. H.; Li, X. P.; Yang, H. B. Hierarchical self-assembly of discrete organoplatinum (II) metallacycles with polysaccharide via electrostatic interactions and their application for heparin detection. *J. Am. Chem. Soc.* **2015**, *137*, 11725−11735.
(45) Zhu, M. H.; Han, S. C.; Liu, J. R.; Tan, M. J.; Wang, W.; Suzuki, K.; Yin, P. C.; Xia, D. B.; Fang, X. K. {Mo126W30}: Polyoxometalate

https://doi.org/10.1021/jacsau.3c00365
JACS Au 2023, 3, 2566−2577

Cages Shaped by π-π Interactions. *Angew. Chem., Int. Ed.* **2022**, *61*, No. e202213910.
(46) Leung, F. C. M.; Leung, S. Y. L.; Chung, C. Y. S.; Yam, V. W. W. Metal-metal and π-π interactions directed end-to-end assembly of gold nanorods. *J. Am. Chem. Soc.* **2016**, *138*, 2989−2992.
(47) Wang, C. X.; Ma, C. K. D.; Yeon, H.; Wang, X. G.; Gellman, S. H.; Abbott, N. L. Nonadditive interactions mediated by water at chemically heterogeneous surfaces: nonionic polar groups and hydrophobic interactions. *J. Am. Chem. Soc.* **2017**, *139*, 18536−18544.
(48) Sánchez-Iglesias, A.; Grzelczak, M.; Altantzis, T.; Goris, B.; Perez-Juste, J.; Bals, S.; Van Tendeloo, G.; Donaldson Jr, S. H.; Chmelka, B. F.; Israelachvili, J. N.; et al. Hydrophobic interactions modulate self-assembly of nanoparticles. *ACS Nano* **2012**, *6*, 11059−11065.
(49) Nummelin, S.; Kommeri, J.; Kostiainen, M. A.; Linko, V. Evolution of structural DNA nanotechnology. *Adv. Mater.* **2018**, *30*, 1703721.
(50) Lacroix, A.; Sleiman, H. F. DNA nanostructures: current challenges and opportunities for cellular delivery. *ACS Nano* **2021**, *15*, 3631−3645.
(51) Li, F.; Li, J.; Dong, B. J.; Wang, F.; Fan, C. H.; Zuo, X. L. DNA nanotechnology-empowered nanoscopic imaging of biomolecules. *Chem. Soc. Rev.* **2021**, *50*, 5650−5667.
(52) Chen, X.; Wang, Y.; Dai, X.; Ding, L.; Chen, J.; Yao, G.; Liu, X.; Luo, S.; Shi, J.; Wang, L.; Nechushtai, R.; Pikarsky, E.; Willner, I.; Fan, C.; Li, J. Single-stranded DNA-encoded gold nanoparticle clusters as programmable enzyme equivalents. *J. Am. Chem. Soc.* **2022**, *144*, 6311−6320.
(53) Yang, Y.; Wu, Z. Y.; Wang, L.; Zhou, K. F.; Xia, K.; Xiong, Q. C.; Liu, L. F.; Zhang, Z.; Chapman, E. R.; Xiong, Y.; et al. Sorting sub-150-nm liposomes of distinct sizes by DNA-brick-assisted centrifugation. *Nat. Chem.* **2021**, *13*, 335−342.
(54) Yao, G. B.; Zhang, F.; Wang, F.; Peng, T.; Liu, H.; Poppleton, E.; Šulc, P.; Jiang, S. X.; Liu, L.; Gong, C.; Jing, X. X.; Liu, X. G.; Wang, L. H.; Liu, Y.; Fan, C. H.; et al. Meta-DNA structures. *Nat. Chem.* **2020**, *12*, 1067−1075.
(55) Madsen, M.; Gothelf, K. V. Chemistries for DNA nanotechnology. *Chem. Rev.* **2019**, *119*, 6384−6458.
(56) Chen, M. M.; Liu, D. P.; Liu, F. S.; Wu, Y. N.; Peng, X. J.; Song, F. L. Recent advances of redox-responsive nanoplatforms for tumor theranostics. *J. Controlled Release* **2021**, *332*, 269−284.
(57) Quinn, J. F.; Whittaker, M. R.; Davis, T. P. Glutathione responsive polymers and their application in drug delivery systems. *Polym. Chem.* **2017**, *8*, 97−126.
(58) Yan, A.; Chen, X. Q.; He, J.; Ge, Y. F.; Liu, Q.; Men, D.; Xu, K.; Li, D. Phosphorothioated DNA Engineered Liposomes as a General Platform for Stimuli-Responsive Cell-Specific Intracellular Delivery and Genome-Editing. *Angew. Chem., Int. Ed.* **2023**, *62*, e202303973.
(59) Cao, Z. H.; Tong, R.; Mishra, A.; Xu, W. C.; Wong, G. C.; Cheng, J. J.; Lu, Y. Reversible cell-specific drug delivery with aptamer-functionalized liposomes. *Angew. Chem., Int. Ed.* **2009**, *48*, 6494−6498.
(60) Wang, M. N.; Chen, Y.; Cai, W. J.; Feng, H.; Du, T. Y.; Liu, W. W.; Jiang, H.; Pasquarelli, A.; Weizmann, Y.; Wang, X. M. In situ self-assembling Au-DNA complexes for targeted cancer bioimaging and inhibition. *Proc. Natl. Acad. Sci. U.S.A.* **2020**, *117*, 308−316.
(61) Wahane, A.; Waghmode, A.; Kapphahn, A.; Dhuri, K.; Gupta, A.; Bahal, R. Role of lipid-based and polymer-based non-viral vectors in nucleic acid delivery for next-generation gene therapy. *Molecules* **2020**, *25*, 2866.
(62) Maugeri, M.; Nawaz, M.; Papadimitriou, A.; Angerfors, A.; Camponeschi, A.; Na, M. L.; Hölttä, M.; Skantze, P.; Johansson, S.; Sundqvist, M.; et al. Linkage between endosomal escape of LNP-mRNA and loading into EVs for transport to other cells. *Nat. Commun.* **2019**, *10*, 4333.
(63) Mendes, B. B.; Conniot, J.; Avital, A.; Yao, D. B.; Jiang, X. Y.; Zhou, X.; Sharf-Pauker, N.; Xiao, Y. L.; Adir, O.; Liang, H. J.; et al. Nanodelivery of nucleic acids. *Nat. Rev. Methods. Primers.* **2022**, *2*, 24.
(64) Ouyang, X. Y.; Wang, M. F.; Guo, L. J.; Cui, C. J.; Liu, T.; Ren, Y. A.; Zhao, Y.; Ge, Z. L.; Guo, X. Q.; Xie, G.; Li, J.; Fan, C. H.; Wang, L. H. DNA Nanoribbon-Templated Self-Assembly of Ultrasmall Fluorescent Copper Nanoclusters with Enhanced Luminescence. *Angew. Chem., Int. Ed.* **2020**, *59*, 11836−11844.
(65) Walsh, A. S.; Yin, H.; Erben, C. M.; Wood, M. J.; Turberfield, A. J. DNA cage delivery to mammalian cells. *ACS Nano* **2011**, *5*, 5427−5432.
(66) Liang, L.; Li, J.; Li, Q.; Huang, Q.; Shi, J. Y.; Yan, H.; Fan, C. H. Single-particle tracking and modulation of cell entry pathways of a tetrahedral DNA nanostructure in live cells. *Angew. Chem., Int. Ed.* **2014**, *53*, 7745−7750.
(67) Ouyang, X. Y.; Li, J.; Liu, H. J.; Zhao, B.; Yan, J.; Ma, Y. Z.; Xiao, S. J.; Song, S. P.; Huang, Q.; Chao, J.; Fan, C. H. Rolling circle amplification-based DNA origami nanostructrures for intracellular delivery of immunostimulatory drugs. *Small* **2013**, *9*, 3082−3087.
(68) Ouyang, X. Y.; Wu, Y. L.; Guo, L. J.; Li, L.; Zhou, M.; Li, X. Y.; Liu, T.; Ding, Y. W.; Bu, H. Y.; Xie, G.; Shen, J. L.; Fan, C. H.; Wang, L. H. Self-assembly Induced Enhanced Electrochemiluminescence of Copper Nanoclusters Using DNA Nanoribbon Templates. *Angew. Chem., Int. Ed.* **2023**, *62*, No. e202300893.
(69) Gibson, D. W.; Beer, M.; Barrnett, R. J. Gold (III) complexes of adenine nucleotides. *Biochem.* **1971**, *10*, 3669−3679.
(70) Shaikh, S.; Rehman, F. U.; Du, T. Y.; Jiang, H.; Yin, L. H.; Wang, X. M.; Chai, R. J. Real-time multimodal bioimaging of cancer cells and exosomes through biosynthesized iridium and iron nanoclusters. *ACS Appl. Mater. Interfaces.* **2018**, *10*, 26056−26063.
(71) Wang, J. L.; Zhang, G.; Li, Q. W.; Jiang, H.; Liu, C. Y.; Amatore, C.; Wang, X. M. In vivo self-bio-imaging of tumors through in situ biosynthesized fluorescent gold nanoclusters. *Sci. Rep.* **2013**, *3*, 1157.
(72) Gao, S. P.; Chen, D. H.; Li, Q. W.; Ye, J.; Jiang, H.; Amatore, C.; Wang, X. M. Near-infrared fluorescence imaging of cancer cells and tumors through specific biosynthesis of silver nanoclusters. *Sci. Rep.* **2014**, *4*, 1−6.
(73) Dunn, K. W.; Kamocka, M. M.; McDonald, J. H. A practical guide to evaluating colocalization in biological microscopy. *Am. J. Physiol. Cell Physiol.* **2011**, *300*, C723−C742.
(74) Zeng, Y.; Qiu, Y.; Jiang, W. L.; Shen, J. Y.; Yao, X. H.; He, X. L.; Li, L.; Fu, B. M.; Liu, X. H. Biological features of extracellular vesicles and challenges. *Front. Cell Dev. Biol.* **2022**, *10*, 1210.
(75) Li, S. W.; Guo, S. J.; Yang, H. L.; Gou, G. L.; Ren, R.; Li, J.; Dong, Z. P.; Jin, J.; Ma, J. T. Enhancing catalytic performance of Au catalysts by noncovalent functionalized graphene using functional ionic liquids. *J. Hazard. Mater.* **2014**, *270*, 11−17.
(76) Song, J. H.; Zhi, G. L.; Zhang, Y.; Mei, B. C. Synthesis and Characterization of CaF_2 Nanoparticles with Different Doping Concentrations of Er^{3+}. *Nano-Micro Lett.* **2011**, *3*, 73−78.
(77) He, X.; Fu, L. J.; Yang, H. M. Insight into the nature of Au-Au_2O_3 functionalized palygorskite. *Appl. Clay. Sci.* **2014**, *100*, 118−122.
(78) Weiher, N.; Willneff, E.; Figulla-Kroschel, C.; Jansen, M.; Schroeder, S. Extended X-ray absorption fine-structure (EXAFS) of a complex oxide structure: a full multiple scattering analysis of the Au L3-edge EXAFS of Au_2O_3. *Solid State Commun.* **2003**, *125*, 317−322.
(79) Li, J.; Yu, J. T.; Huang, Y. S.; Zhao, H. R.; Tian, L. L. Highly stable and multiemissive silver nanoclusters synthesized in situ in a DNA hydrogel and their application for hydroxyl radical sensing. *ACS Appl. Mater. Interfaces.* **2018**, *10*, 26075−26083.
(80) Zhang, J.; Chen, R.; Zhu, Z.; Adachi, C.; Zhang, X.; Lee, C.-S. Highly Stable Near-Infrared Fluorescent Organic Nanoparticles with a Large Stokes Shift for Noninvasive Long-Term Cellular Imaging. *ACS Appl. Mater. Interfaces.* **2015**, *7*, 26266−26274.
(81) Zhu, J. Y.; He, K.; Dai, Z. Y.; Gong, L. S.; Zhou, T. Y.; Liang, H. R.; Liu, J. B. Self-assembly of luminescent gold nanoparticles with sensitive pH-stimulated structure transformation and emission response toward lysosome escape and intracellular imaging. *Anal. Chem.* **2019**, *91*, 8237−8243.

https://doi.org/10.1021/jacsau.3c00365
JACS Au 2023, 3, 2566−2577

(82) Balfourier, A.; Luciani, N.; Wang, G.; Lelong, G.; Ersen, O.; Khelfa, A.; Alloyeau, D.; Gazeau, F.; Carn, F. Unexpected intracellular biodegradation and recrystallization of gold nanoparticles. *Proc. Natl. Acad. Sci. U.S.A.* **2020**, *117*, 103−113.
(83) Mu, W. Y.; Yang, R.; Robertson, A.; Chen, Q. Y. A near-infrared BSA coated DNA-AgNCs for cellular imaging. *Colloid Surface B* **2018**, *162*, 427−431.

https://doi.org/10.1021/jacsau.3c00365
JACS Au 2023, 3, 2566−2577